

RESEARCH ARTICLE

10.1002/2016JC011720

Key Points:

- *Microcystis* vertical distribution is a dynamic balance between turbulence and buoyancy
- Appropriate time step and numerical scheme avoid artifacts in random walk models
- Vertical mixing with buoyancy improved simulation of bloom spatial distribution

Correspondence to:

M. D. Rowe,
mark.rowe@noaa.gov

Citation:

Rowe, M. D., E. J. Anderson, T. T. Wynne, R. P. Stumpf, D. L. Fanslow, K. Kijanka, H. A. Vanderploeg, J. R. Strickler, and T. W. Davis (2016), Vertical distribution of buoyant *Microcystis* blooms in a Lagrangian particle tracking model for short-term forecasts in Lake Erie, *J. Geophys. Res. Oceans*, 121, 5296–5314, doi:10.1002/2016JC011720.

Received 12 FEB 2016

Accepted 23 JUN 2016

Accepted article online 27 JUN 2016

Published online 31 JUL 2016

Vertical distribution of buoyant *Microcystis* blooms in a Lagrangian particle tracking model for short-term forecasts in Lake Erie

M. D. Rowe¹, E. J. Anderson², T. T. Wynne³, R. P. Stumpf³, D. L. Fanslow², K. Kijanka¹, H. A. Vanderploeg², J. R. Strickler⁴, and T. W. Davis²

¹University of Michigan, Cooperative Institute for Limnology and Ecosystems Research (CILER), NOAA Great Lakes Environmental Research Laboratory, Ann Arbor, Michigan, USA, ²Great Lakes Environmental Research Laboratory, Oceanic and Atmospheric Research, National Oceanic and Atmospheric Administration, Ann Arbor, Michigan, USA, ³National Centers for Coastal Ocean Science, National Ocean Service, National Oceanic and Atmospheric Administration, Silver Spring, Maryland, USA, ⁴Great Lakes WATER Institute, University of Wisconsin—Milwaukee, Milwaukee, Wisconsin, USA

Abstract Cyanobacterial harmful algal blooms (CHABs) are a problem in western Lake Erie, and in eutrophic fresh waters worldwide. Western Lake Erie is a large (3000 km²), shallow (8 m mean depth), freshwater system. CHABs occur from July to October, when stratification is intermittent in response to wind and surface heating or cooling (polymictic). Existing forecast models give the present location and extent of CHABs from satellite imagery, then predict two-dimensional (surface) CHAB movement in response to meteorology. In this study, we simulated vertical distribution of buoyant *Microcystis* colonies, and 3-D advection, using a Lagrangian particle model forced by currents and turbulent diffusivity from the Finite Volume Community Ocean Model (FVCOM). We estimated the frequency distribution of *Microcystis* colony buoyant velocity from measured size distributions and buoyant velocities. We evaluated several random-walk numerical schemes to efficiently minimize particle accumulation artifacts. We selected the Milstein scheme, with linear interpolation of the diffusivity profile in place of cubic splines, and varied the time step at each particle and step based on the curvature of the local diffusivity profile to ensure that the Visser time step criterion was satisfied. Inclusion of vertical mixing with buoyancy significantly improved model skill statistics compared to an advection-only model, and showed greater skill than a persistence forecast through simulation day 6, in a series of 26 hindcast simulations from 2011. The simulations and in situ observations show the importance of subtle thermal structure, typical of a polymictic lake, along with buoyancy in determining vertical and horizontal distribution of *Microcystis*.

1. Introduction

Harmful algal blooms (HABs) are a global problem that is linked to anthropogenic eutrophication of inland and coastal waters, and may be exacerbated by climate change [O'Neil *et al.*, 2012]. Lake Erie has experienced recurring blooms of toxin-producing cyanobacteria since the mid-1990s [Brittain *et al.*, 2000; Michalak *et al.*, 2013; Wynne and Stumpf, 2015]. Lake Erie is the most productive, warm, and shallow of the Laurentian Great Lakes of North America. In the open waters of Lake Erie, cyanobacterial harmful algal blooms (CHABs) generally occur from July to October, and are dominated by the species *Microcystis aeruginosa*, which produces the group of hepatotoxin compounds known as microcystins [Rinta-Kanto *et al.*, 2009]. CHABs occur primarily in the shallow western basin, which receives the main hydraulic load from the Detroit River in the north and the main nutrient load from the Maumee River [Kane *et al.*, 2014] in the southwest (Figure 1a). Occasionally, CHABs are transported through the islands into the deeper central basin, while the eastern basin is largely free of CHABs (Figure 1a) [Wynne and Stumpf, 2015]. A bloom of record-breaking intensity and extent occurred in 2011. Analysis by Michalak *et al.* [2013] indicated that the conditions of meteorology and agricultural land use that caused the 2011 record bloom are likely to recur, and the 2015 bloom subsequently exceeded the severity of the 2011 record bloom [Stumpf and Wynne, 2015].

Forecasts of CHAB abundance and spatial distribution are useful to water treatment plant operators, anglers, recreational boaters, and beach users. Lake Erie is a source of drinking water to 11 million people [Lake Erie

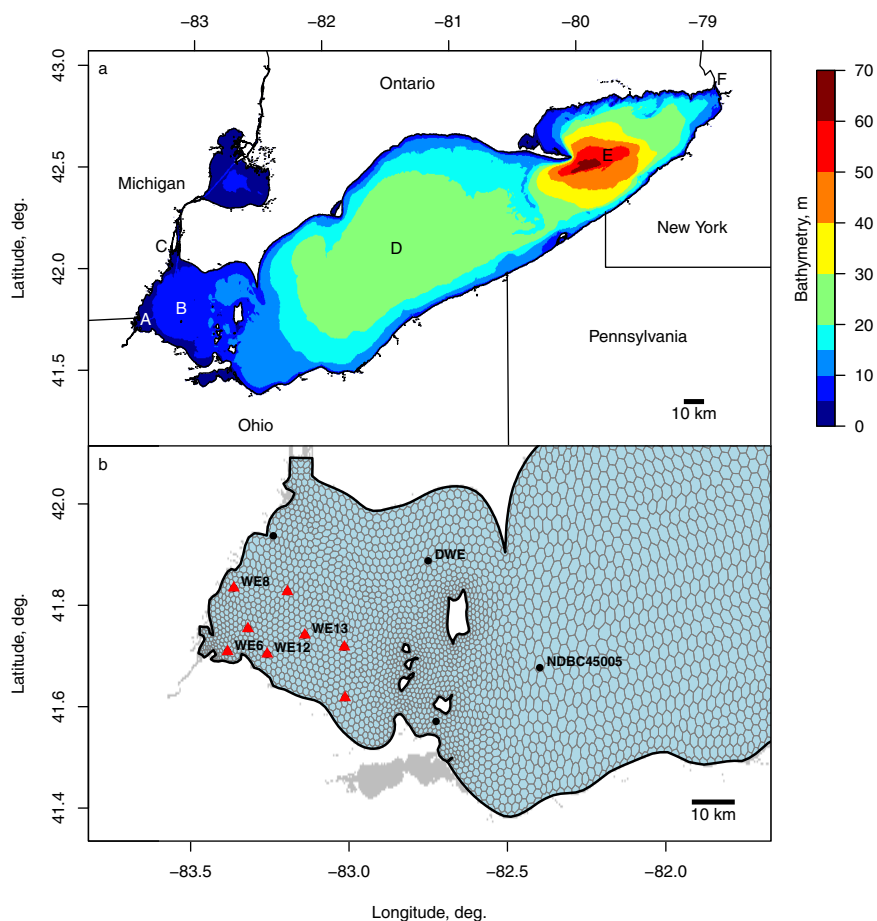


Figure 1. (a) Geographic location and bathymetry of Lake Erie, showing bordering United States and the Canadian province of Ontario. Features of interest are identified, including (A) Maumee Bay, (B) Western Basin, (C) Gibraltar on the Detroit River, (D) Central Basin, (E) Eastern Basin, and (F) Buffalo on the Niagara River. (b) An enlarged view of the western portion of the FVCOM model domain. FVCOM domain boundaries are indicated with a heavy black line, and node-centered tracer control elements with gray lines. Surface mixed layer depth was estimated in hindcast simulations at the stations identified with symbols. Well-mixed condition simulations were conducted at the named stations. Profiles of temperature and cyanobacterial chlorophyll concentration were measured at the stations indicated by red triangles.

LaMP, 2011]. In 2014, the City of Toledo issued a do-not-drink order that affected a half million residents for two days as a result of contamination of treated water by microcystins [Henry, 2014]. In addition to spatial forecasts, forecasts of *Microcystis* vertical distribution are of interest to water treatment plant operators because intake structures are usually located subsurface, so the risk of toxins in their raw water may be greater during mixing events than when *Microcystis* colonies are concentrated on the surface. In addition to providing drinking water, Lake Erie supports economically valuable sport and commercial fisheries as well as recreation and tourism.

Short-term and seasonal CHAB forecasts have been developed for Lake Erie. Seasonal forecasts predict the annual bloom severity using statistical models based on the cumulative March to July phosphorus load from the Maumee River, which are able to explain >90% of the interannual variance in bloom severity [Obenour *et al.*, 2014]. Bloom severity is defined as the lake-wide cyanobacterial biomass averaged over the 30 days containing the maximum biomass [Obenour *et al.*, 2014; Stumpf *et al.*, 2012], and has been estimated using both satellite [Stumpf *et al.*, 2012] and plankton tow data [Bridgeman *et al.*, 2013]. The seasonal forecast is used by water treatment plant managers for seasonal planning, to determine recommended phosphorus load reductions to meet commitments under the Great Lakes Water Quality Agreement [GLWQA Annex 4, 2015], and is distributed to over 1600 subscribers. Short-term forecasts are distinct from the seasonal forecast in the greater importance of physical transport processes over biological mechanisms in explaining short-term bloom variability. Experimental short-term forecasts have been developed for Lake Erie that indicate the present location and extent of CHABs from satellite imagery, then predict future movement of the CHAB using forecast

meteorology, a hydrodynamic model, and a Lagrangian particle tracking model to simulate horizontal advection of neutrally-buoyant particles at the water surface [Wynne *et al.*, 2013, 2011].

Skill assessment of short-term CHAB forecasts is needed so that forecast users may have an appropriate level of confidence in forecast data, and for development of improved models. However, CHAB forecast skill assessment can be challenging, and methods are not well established. Wynne *et al.* [2011] showed that a forecast model more accurately predicted horizontal movement of the bloom centroid (center of mass) than a persistence forecast over a ten-day simulation for an August 2003 event. A persistence forecast is a benchmark used for model skill assessment in which no change is assumed from the initial observed location. The same quantitative skill assessment method could not be applied in the case of an August 2008 event because cloud cover and vertical mixing obscured parts of the bloom in subsequent images and prevented an accurate estimate of the centroid location [Wynne *et al.*, 2011]. In a detailed analysis of the August 2008 bloom in Lake Erie, Wynne *et al.* [2010] found that wind speed was a significant predictor of apparent bloom intensity in satellite imagery, and presented evidence to support the hypothesis that variation in the mixing depth of the buoyant cyanobacterial colonies was the underlying mechanism causing changes in surface concentration. In a qualitative analysis of the first 3 years of the experimental Lake Erie CHAB forecast (2008–2010), Wynne *et al.* [2013] concluded that the forecast provided useful information, but could be improved by a means to fill in cloud-covered areas in the satellite images, and by simulation of vertical mixing of the buoyant cyanobacteria.

To simulate concentration profiles of buoyant particles produced by vertical mixing in stratified turbulence, the partial differential equations governing advection and diffusion may be solved from an Eulerian or a Lagrangian perspective; each approach has strengths and weaknesses. Real phytoplankton communities have properties that vary among individuals within a population, such as size, specific gravity, light exposure history, and nutrient quotas. A strength of Lagrangian particle models is that nearly continuous distributions of properties can be represented by allowing properties to vary by particle [e.g., Ross and Sharples, 2008], while in Eulerian models property distributions are usually represented by a limited number of discrete property classes [e.g., Medrano *et al.*, 2013].

A weakness of the Lagrangian approach is that artificial accumulation of particles can occur in low diffusivity areas in random-walk turbulence simulations for the case of spatially (vertically) nonuniform diffusivity if an inappropriate numerical scheme or time step is used [Visser, 1997]. These artifacts can be easy to misinterpret as features of interest. Several studies have applied Lagrangian particle models to the 1-D column case with steady, idealized diffusivity profiles [Gräwe *et al.*, 2012; Ross and Sharples, 2008; Visser, 1997]. In 3-D ocean and lake models, use of random-walk vertical mixing schemes can be challenging because the required time step varies spatially and temporally over the model domain. A fixed time step may be selected that is adequate in most places and times [Huret *et al.*, 2007], or in some cases a well-mixed profile was imposed in shallow regions where a small time step would be required to avoid formation of artifacts [Gilbert *et al.*, 2010]. Our application required realistic rather than idealized diffusivity profiles for a polymictic lake in which conditions are alternately turbulent and stratified, and to simulate concentration profiles rather than specify a well-mixed condition, even in shallow areas, therefore some development of the random-walk approach was required.

We describe a short-term forecast system for CHAB abundance and distribution in Lake Erie that takes a similar approach to that of Wynne *et al.* [2011], but uses updated hydrodynamic and Lagrangian particle tracking models, and includes a means of filling in cloud-covered areas of satellite images using model data from a previous run. In addition, we describe a method to simulate vertical distribution of buoyant cyanobacteria in stratified turbulence. We evaluated the performance of several random-walk turbulence numerical schemes in terms of computational efficiency and their ability to minimize artifacts in simulations with vertically varying diffusivity typical of a large polymictic lake. We compared simulated vertical distributions of cyanobacteria to observed profiles in Lake Erie. Finally, we show that model skill statistics were improved by including vertical mixing with buoyancy in hindcast simulations of the spatial distribution of the 2011 bloom in Lake Erie.

2. Methods

2.1. Hydrodynamic Model

The Finite Volume Community Ocean Model (FVCOM, v. 3.2) is an unstructured grid, finite-volume, free surface, three-dimensional primitive equation ocean model that solves the momentum, continuity, temperature, salinity, and density equations [Chen *et al.*, 2003]. Turbulence closure is implemented through the

MY-2.5 scheme for vertical mixing [Galperin *et al.*, 1988], and the Smagorinsky scheme for horizontal mixing [Smagorinsky, 1963]. FVCOM has been adapted and implemented for the Great Lakes in several recent studies [Anderson *et al.*, 2015; Anderson and Schwab, 2013; Anderson *et al.*, 2010; Bai *et al.*, 2013], yielding accurate predictions of temperature, water levels, and currents. In particular, FVCOM has been applied to Lake Erie for extreme storm prediction [Anderson *et al.*, 2015] and serves as the oceanographic model underlying NOAA's next-generation Lake Erie Operational Forecast System (LEOFS), a real-time short-term hydrodynamic forecast model (<http://tidesandcurrents.noaa.gov/ofs/leofs/leofs.html>).

The FVCOM-based LEOFS model was applied for this study with bathymetry interpolated from the NOAA National Geophysical Data Center. (www.ngdc.noaa.gov/mgg/greatlakes/greatlakes.html). The unstructured grid consisted of 6106 nodes and 11,509 elements (Figure 1). Spatial resolution was 2 km in the central basin, 1.5 km in the western basin, and 0.5 km in Maumee Bay and the islands (Figure 1b) to improve representation of currents in these key areas for CHAB transport, with 20 uniform vertical sigma layers.

Dynamic water levels (6 min) were prescribed at open boundaries at the Detroit River and the Niagara River, taken from adjustments to the NOAA/NOS gauges at Gibraltar (9044020) and Buffalo (9063020), to drive the primary inflow and outflow, respectively (Figure 1a). Atmospheric forcing conditions were generated using station-based interpolation methods as in the NOAA Great Lakes Coastal Forecasting System [Beletsky *et al.*, 2003]. Hourly meteorological forcing variables of wind speed, wind direction, air temperature, dewpoint temperature, and cloud cover were interpolated over Lake Erie from several land-based meteorological stations and offshore NOAA/NDBC buoys (45004, 45132, and 45142), when available. Wind speeds were adjusted to 10 m height and empirical relationships were used to adjust land-based meteorological variables for over-lake modification [Beletsky *et al.*, 2003].

Hydrodynamic model simulations were based on the real-time LEOFS nowcast, which was initialized on 1 January 2004 with uniform temperature of 2°C. For the 2011 scenario presented here, the hydrodynamic model simulation was initialized on 1 January 2011 with initial conditions provided by the simulation from the previous year, and produced hourly output of three-dimensional currents, water temperature, turbulent diffusivity, and 2-D water level fluctuations.

2.2. Lagrangian Particle Tracking Model

Lagrangian particle tracking was accomplished using a Fortran program developed previously to study transport of larval cod in the Gulf of Maine [Churchill *et al.*, 2011; Huret *et al.*, 2007], which is distributed as part of the FVCOM code package (<http://fvcom.smast.umassd.edu/>), and has previously been applied in the Great Lakes [Anderson and Phanikumar, 2011]. Advection of particles was determined by

$$\frac{d}{dt}\mathbf{X}(t)=\mathbf{V}(\mathbf{X}(t),t) \quad (1)$$

where $\mathbf{X}(t)$ is the three-dimensional particle position at time t , and $\mathbf{V}(\mathbf{X}(t),t)$ is the three-dimensional, time varying velocity field. Linear interpolation in space and time was used to obtain $\mathbf{V}(\mathbf{X}(t),t)$ from hourly archived FVCOM output. The contribution of advection to the particle position was updated by integrating equation (1) using an explicit fourth-order Runge-Kutta scheme with a time step, $\Delta t = 600$ s. Vertical mixing due to turbulent eddy diffusivity was optionally simulated using one of several random-walk schemes, described below. We used reflected boundary conditions at vertical and horizontal boundaries in all simulations.

2.3. Well-Mixed Condition Test

We compared the performance of several random walk vertical mixing numerical schemes using a well-mixed condition test case [Visser, 1997] that can be used to evaluate whether a given numerical scheme and time step will produce artifacts in simulated concentration profiles. In our case, the well-mixed condition simulation was performed by initiating 1000 particles, uniformly distributed through the water column, then simulating 1-D vertical mixing with neutral buoyancy using time series of Lake Erie diffusivity profiles output from FVCOM for the month of August 2011 (Table 1). Random noise in the simulated concentration profiles decreases with increasing number of particles, and 1000 particles were found to be adequate in 1-D simulations [Ross, and Sharples, 2004]. These simulations are expected to give uniform concentration at all time regardless of the diffusivity profile, consistent with the Eulerian solution to the 1-D diffusion equation with initial uniform concentration [Visser, 1997].

Table 1. Dates of Measurements and Model Simulations

Measurement or simulation	Date
Well-mixed condition simulations	Aug 2011
Satellite images, 2-D, 3-D simulations	26 dates, Jul to Oct 2011
Colony size distribution (FlowCam)	4 Aug 2014
Colony size distribution (microscopy)	Weekly sampling Jul to Sep 2012 and 2013
Buoyant velocity measurements	15 and 21 Jul 2015
Vertical profiles (FluoroProbe)	Weekly sampling Jul to Sep 2015

To evaluate performance in the well-mixed condition test in a way that is directly relevant to our application, we defined a signal-to-noise ratio, SN , based on simulated surface concentration,

$$SN(t) = C(t) / |1.0 - C_{wm}(t)| \quad (2)$$

where $C_{wm}(t)$ is the time-dependent concentration in the 1 m thick surface layer,

normalized to the column-mean concentration, in a well-mixed condition simulation with neutral buoyancy. A constant value of 1.0 is expected for $C_{wm}(t)$, therefore $|1.0 - C_{wm}(t)|$ represents the magnitude of “noise” due to artifacts and random fluctuations due to calculating concentration by counting discrete particles in a control volume. The “signal” is provided by the analogous surface concentration, $C(t)$, from an identical simulation *with* buoyancy. A large value of SN indicates that artifacts are small compared to the effect of interest, which is the fluctuation in surface concentration due to buoyancy. SN can be made arbitrarily large by using a small time step and a large number of particles, but at the expense of computational time. We selected a value of 5 as a goal minimum value for SN , based on the “Rose criterion” for the detection limit of the human eye for image features [Rose, 1948]. Accordingly, we used the frequency of occurrence of $SN < 5$ over the hourly records in a simulation as the performance criterion by which to evaluate the numerical schemes and time step criteria.

2.4. Random Walk Vertical Mixing Schemes

We evaluated the Visser [1997] scheme, as implemented by Huret *et al.* [2007]

$$z(t + \delta t) = z(t) + w_b \delta t + K(z(t)) \delta t + R \sqrt{\frac{2K(\bar{z}) \delta t}{\sigma^2}} \quad (3)$$

where $z(t)$ is the vertical position of the particle at time t , δt is the vertical random walk time step, w_b is a floating/sinking/swimming vertical velocity component, K is the vertical turbulent diffusivity, $K' = dK/dz$, R is a random variable sampled from a uniform distribution with zero mean and standard deviation σ , and $\bar{z} = z(t) + 0.5K'(z(t))\delta t$ is a vertical position displaced from the particle position as a function of the diffusivity gradient. Following Ross and Sharples [2004], a cubic spline interpolation was used to obtain a continuous, differentiable diffusivity profile.

In addition to the Visser scheme, described above, we evaluated random walk vertical mixing schemes with higher order accuracy including the Milstein, Strong 1.5 (S1.5), and Platen two-step (PC2) schemes that were implemented in Fortran for the General Ocean Turbulence Model by Gräwe [2011]. After evaluating the performance of 10 random walk schemes [Gräwe, 2011], Gräwe *et al.* [2012] recommended the use of either the Milstein scheme or higher order schemes such as S1.5 or PC2. The order of accuracy (rate of convergence) of numerical approximations to stochastic differential equations is separated into weak and strong cases, where the weak case relates to the accuracy of the ensemble particle distribution, while the strong case relates to the accuracy of particle trajectories [Gräwe, 2011]. The weak order of accuracy of the schemes that we evaluated was 1 for Visser and Milstein and 2 for S1.5 and PC2. The strong order of accuracy was 1 for Milstein, 1.5 for S1.5, and was not defined for Visser or PC2 [Gräwe, 2011]. The Milstein scheme is

$$z(t + \delta t) = z(t) + w_b \delta t + 0.5K'(z(t)) [\Delta W^2 + \delta t] + \Delta W \sqrt{2K(z(t))} \quad (4)$$

where ΔW is a random variable drawn from a Gaussian distribution with zero mean and standard deviation $\sqrt{\delta t}$. Because the Milstein scheme is first order, linear interpolation of the diffusivity profile to obtain $K(z(t))$ and $K'(z(t))$ are sufficient, and the added computational expense compared to the Visser scheme (equation (3)) is minimal. The second-order schemes S1.5 and PC2 retain additional terms from the stochastic Taylor expansion, including higher order derivatives that require the application of cubic splines to the diffusivity profile, and S1.5 requires an additional random variable, therefore the second-order schemes have greater computational expense. We refer to Gräwe [2011] for a full explanation of the S1.5 and PC2 schemes.

2.5. Random Walk Time Step

Visser [1997] introduced a time step criterion, $\delta t \ll \min(1/|K''|)$, where K'' is the second derivative of the diffusivity profile, so that the diffusivity profile is reasonably approximated by a first-order Taylor series expansion over the range of particle displacement. Ross and Sharples [2004] found that

$$\delta t = \frac{1}{100|K''|} \quad (5)$$

is acceptable in most applications. To ensure the use of an appropriate time step throughout a 3-D model domain, and to avoid the need to specify an appropriate δt in advance, we modified the code of Huret *et al.* [2007] to allow an appropriate value of δt to be calculated and applied for each particle at each δt . To evaluate equation (5) independently of spline interpolation, we calculated K'' directly at the FVCOM sigma levels using a centered finite difference approximation, and extended the profile beyond the surface and bottom by reflection. We further limited $0.01 \leq \delta t \leq \Delta t$. We tracked the minimum δt during simulations to confirm that the lower limit of 0.01 s was rarely applied.

2.6. Measurement of *Microcystis* Colony Size Distribution

We assigned buoyant velocity in the model based on measured size distributions and regressions of buoyant velocity versus colony diameter. We measured *Microcystis* colony diameter of Lugol preserved samples collected from western Lake Erie in the summers of 2012, 2013, and 2014. In 2012 and 2013, colony diameters were measured by microscopy (Table 1). In 2014, we used the FlowCam (Fluid Imaging Technologies). The FlowCam captures images of individual colonies and estimates their equivalent spherical diameter by image analysis. Wang *et al.* [2015] showed that counts and colony diameters of *Microcystis* given by FlowCam and microscopic image analysis diameters were nearly identical. Colonies in Lake Erie are typically $>50 \mu\text{m}$ [Vanderploeg *et al.*, 2001] and buoyant. Samples were preserved with 1% formalin upon collection, immediately refrigerated, and analyzed within 24 h. FlowCam analyses were performed with a $2\times$ objective and $1 \times 3 \text{ mm}$ field of view flow cell with samples diluted as per manufacturer recommendations to avoid capturing more than one image per trigger event. Fluorescent triggering mode was used to avoid imaging detrital material that might be confused with *Microcystis*. Samples were diluted in $0.2 \mu\text{m}$ filtered algal culture media [e.g., Vanderploeg, *et al.*, 2001] and injected into the FlowCam with a 60 mL syringe, which was constantly turned over so as to prevent the buoyant colonies from aggregating in the syringe. The image analysis algorithm was calibrated to identify the colony outline including the mucilage.

2.7. Measurement of *Microcystis* Colony Buoyant Velocity

Microcystis colony buoyant velocity was measured using microscopic videography [Bundy *et al.*, 1998; Strickler, 1985], a method in principle similar to that of Nakamura *et al.* [1993]. Surface water samples were collected on 15 and 21 July 2015 (Table 1) at station WE15 (Figure 1b, $-83.0, 41.6$) during the early afternoon. Water was placed in 1 L glass bottles in an incubator outdoors with a neutral density filter to cut light intensity to 50% of surface irradiance. Measurements of colony velocities were made throughout the morning and afternoon of the next day. Digital video clips were captured of individual colonies rising through a $2 \text{ cm} \times 2 \text{ cm}$ cross section $\times 30 \text{ cm}$ tall glass cuvette filled with ambient lake water inside of a water jacket in a temperature controlled environmental room maintained at the lake temperature. Image capture and analysis software (Templo Motus, Vicon Motus, Contemplas, GmbH, Germany) was used to measure the velocity of the rising colonies. Diameters of the colonies were determined from image analysis of video images using Image-Pro software (Media Cybernetics, Rockville, MD). Water samples were diluted as needed with $0.2 \mu\text{m}$ filtered lake water to avoid turbulence induced by multiple rising colonies.

2.8. Measured Vertical Profiles of Temperature and Cyanobacterial Concentration

Vertical profiles of temperature and cyanobacterial concentration (reported in μg chlorophyll a L^{-1}) were measured using the FluoroProbe (bbe Moldaenke, GmbH), which uses spectral fluorometry to partition total chlorophyll into multiple phytoplankton classes on the basis of their characteristic pigments (green algae, cyanobacteria, diatoms/dinoflagellates, cryptophytes), with correction for possible interference by colored dissolved organic matter [Catherine *et al.*, 2012; Kring *et al.*, 2014]. Standard factory calibration settings for representative algal classes were used. Profiles were measured at 11 stations (Figure 1) weekly from June through September, 2015 (Table 1). Profiles were selected for model skill assessment in which the

cyanobacterial chlorophyll was greater than chlorophyll from other algal classes, which occurred 13 July to 28 September.

2.9. Satellite Remote Sensing Data

To initialize model simulations, and for model skill assessment, we used a series of images of cyanobacterial blooms in Lake Erie from July to October 2011 (Table 1) that were derived from the Medium Resolution Imaging Spectrometer (MERIS) [Wynne and Stumpf, 2015]. MERIS standard level 2 data sets (in units of sr^{-1}) were used with a spectral shape algorithm based around 680 nm [Wynne et al., 2008] to obtain the cyanobacterial index (CI). CI varies linearly with biomass, with a value of 10^{-3}sr^{-1} corresponding to approximately $10^5 \text{ cells mL}^{-1}$ [Stumpf et al., 2012], which is the World Health Organization's threshold of significantly increased risk for human health effects [Chorus and Bartram, 1999]. For our analysis, we converted CI to chlorophyll concentration using an empirical relationship derived from field radiometry and grab sample extracted chlorophyll from eutrophic lakes in Florida (R^2 0.95, std. error $7.7 \mu\text{g L}^{-1}$, range 16 to $115 \mu\text{g L}^{-1}$). The relationship was also verified for satellite-derived CI, and gave a relative root-mean square error of 27% [Tomlinson et al., 2016].

$$\text{Chl} = 12570 \text{ CI} + 10 \quad (6)$$

A value of $\text{CI} = 10^{-3} \text{sr}^{-1}$ is approximately equivalent to $23 \mu\text{g L}^{-1}$ chlorophyll, which we used as a threshold to define the presence of a CHAB.

2.10. Hindcast Simulations

Daily satellite images for the period July to October 2011 were evaluated, and 26 images were selected that had >50% cloud-free views of western Lake Erie. A 10 day model simulation was initialized from each image by assigning surface chlorophyll concentration values to FVCOM nodes by nearest neighbor interpolation. Concentration was converted to Lagrangian particles by specifying a chlorophyll mass per particle ($10^{10} \mu\text{g Chl particle}^{-1}$) and placing the specified number of particles within a control volume. The FVCOM node-centered tracer control elements were used as control volumes (Figure 1). Vertical layers were specified as constant-thickness (1 m) z-layers.

Preliminary hindcast skill assessment indicated a need to censor satellite data within a buffer region of shorelines due to frequent false positives in these areas, which was likely caused by contamination of the water signal from relatively bright surrounding land or by bottom reflectance. The buffer width was set to 1 km south of Stony Point (41.94°Lat.) and east of Catawba Island (-82.85°Lon.) and to 1.5 km elsewhere. The buffer was not applied in Maumee Bay because CHABs were often present [Wynne and Stumpf, 2015], reducing the likelihood of false positives. Buffered or missing data areas were assigned values by nearest neighbor if pixels containing valid data were available within 2 km. If no valid pixels were available within 2 km of a node one of two approaches was used: (1) it was assumed that no CHAB was present ($\text{Chl} = 0$) or (2) model output was carried forward to fill in the no-data area if a previous model run was available covering the time period.

Two types of simulations were run, 2-D and 3-D. In 2-D simulations, the surface chlorophyll concentration was applied to the surface 1 m, with $\text{Chl} = 0$ below, and random walk vertical mixing was turned off. In 3-D simulations, surface chlorophyll concentration was applied over the surface mixed layer (SML) depth (see below), and random walk vertical mixing was simulated. Both 2-D and 3-D simulations included 3-D advection.

2.11. Estimation of the Surface Mixed Layer Depth

It was necessary to estimate the surface mixed layer (SML) depth for buoyant *Microcystis* colonies for the purpose of initializing the vertical distribution of particles (chlorophyll concentration) in 3-D simulations from satellite-derived surface chlorophyll concentration. The vertical distribution of buoyant particles in the water column depends on buoyancy in addition to turbulent diffusivity (e.g., Figures 2d and 2e); therefore, we used the Lagrangian particle model to estimate the initial vertical distribution of *Microcystis* colonies rather than using diffusivity or temperature profiles from FVCOM directly. Initial vertical profiles were simulated at a subset of FVCOM nodes (stations) because a large number of particles is needed to obtain a well-resolved profile, which would be computationally intensive to simulate at all 6106 nodes. The SML depth was estimated by running 1-D column vertical random walk simulations at 11 station locations (Figure 1b)

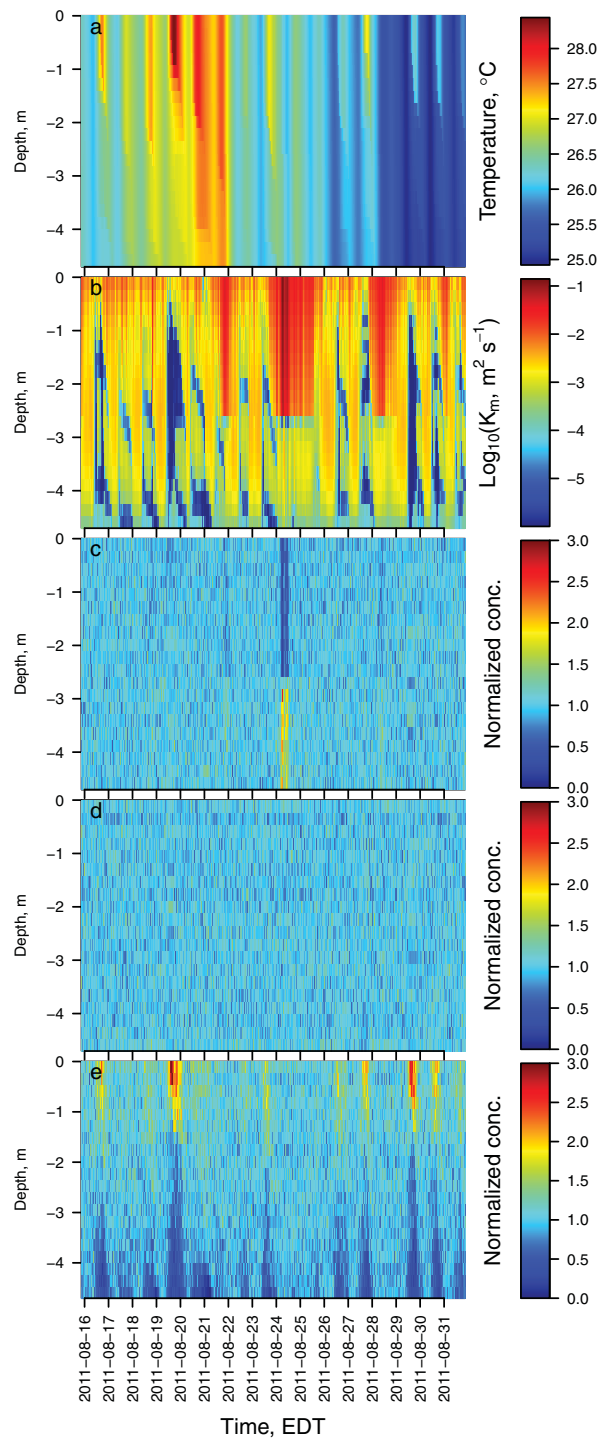


Figure 2. Time series of (a) temperature and (b) diffusivity profiles output from FVCOM for 16–31 August 2011 at station WE8. Time series of normalized concentration profiles from 1-D vertical random walk simulations without buoyancy (well-mixed condition test) using (c) the Visser scheme with fixed 1 s time step, and Visser scheme with variable time step (d) set according to the Visser criterion (equation (5)). (e) A 1-D simulation with buoyancy (N93 3 Aug) using the Visser scheme and variable time step. Artificial accumulation of particles in a low diffusivity area with associated depletion in the upper half of the water column can be seen on 24 August (c), with improved performance from the variable time step (d).

that were selected to provide representative coverage of the western basin where CHABs are most common, with additional stations added at representative deeper locations. 1-D simulations were initialized with 1000 particles uniformly distributed over the column 36 h prior to the initialization time of the 3-D model (satellite image time) to allow the particle distribution sufficient time to adapt to the varying diffusivity. Random walk vertical mixing was forced by hourly diffusivity output from FVCOM. The SML depth for *Microcystis* colonies was estimated as the depth at which the 1-D concentration profile decreased to half the surface concentration, and the satellite-derived surface concentration was applied from the surface to this depth; this approach provides an unbiased estimate of the total column biomass for the case of a uniform concentration profile or a profile that can be approximated by a linear decrease. SML depth was interpolated spatially to the FVCOM nodes by the nearest neighbor method.

2.12. Model Skill Statistics

Comparison of model results to in situ profile data was conducted using column-integrated quantities to minimize the effect of noise in the profile data on the statistics. Turbulent diffusivity is strongly influenced by the static stability of the water column, which can be quantified using the potential energy anomaly, ϕ ,

$$\phi = \frac{1}{h} \int_0^h (\hat{\rho} - \rho)gzdz; \hat{\rho} = \frac{1}{h} \int_0^h \rho dz \quad (7)$$

where ρ is the local density, h is the water column depth, and g is acceleration due to gravity [Simpson and Bowers, 1981; Wiles et al., 2006]. Vertical distribution of concentration was characterized by calculating the center of mass of the normalized concentration profile, σ_m

$$\sigma_m = \frac{1}{C} \sum_{k=1}^{k_b} c_k \sigma_k; C = \sum_{k=1}^{k_b} c_k \quad (8)$$

where $\sigma = z/h$ is the normalized vertical coordinate, c is the concentration at layer k normalized to the column-mean

concentration, and $k_b = 20$ is the number of uniformly-spaced σ layers in the model grid. The observed concentration profile was averaged over the σ layers of the model grid for the purpose of comparison to the model profiles.

Skill assessment in hindcast simulations was conducted by comparing model results to remote sensing images that were within the model simulation period. Each hindcast simulation was initialized from a satellite image, and two to four subsequent images were typically available within the simulation period for skill assessment. Skill assessment was conducted using a binary categorical variable (CHAB, no CHAB), and pixel-by-pixel comparisons of model to remote sensing observations were conducted. FVCOM tracer control elements (Figure 1) were used as the spatial segmentation (pixels).

Our approach to skill assessment statistics followed *Hogan and Mason* [2012]. Two statistics were calculated from the elements of the contingency table, which are the number of a , correctly predicted events (hits); b , false events (false alarms); c , false negatives (misses); and d , correct nonevents. The frequency bias (B) gives the ratio of the number of forecasts of occurrence to the number of observed occurrences

$$B = \frac{a+b}{a+c} \quad (9)$$

and the Pierce skill score (PSS) gives the hit rate minus the false alarm rate.

$$PSS = \frac{ad-bc}{(b+d)(a+c)} \quad (10)$$

An unbiased forecast has a frequency bias $B = 1.0$. PSS values range from -1.0 to 1.0 , with positive values indicating that the hit rate was greater than the false positive rate, and therefore the model had greater skill than a random forecast or constant CHAB or no-CHAB prediction [*Hogan and Mason*, 2012].

To provide a reference forecast for skill comparison, we defined a “persistence” forecast as the assumption of no change from the satellite image that was used to initialize the model, which represents the best available information to a forecast user in the absence of a useful model. We took the further steps of filling in missing data in the persistence forecast with the most recent satellite data for each spatial segment, and applying the same shoreline buffering procedure that was used to initialize the model.

To test whether the model had significantly greater skill than the persistence forecast, we used the bootstrap method described by *Hogan and Mason* [2012] to estimate the confidence interval around the difference in skill score of the model compared to the persistence forecast. Starting with a series of n triplets of observations, model predictions, and persistence predictions, we created 1000 different bootstrap samples, each of length n , by taking random samples with replacement from the series. We then calculated the difference in PSS, ΔPSS , for each bootstrap sample. Finally, we estimated the 95% confidence interval as the 0.025 to 0.975 quantiles of the ensemble of 1000 values of ΔPSS . While analytical formulas are available to estimate the uncertainty in PSS, the bootstrap method accounts for effects of spatial and temporal autocorrelation in environmental data, which effectively reduce the number of independent observations to be $<n$ [*Hogan and Mason*, 2012].

3. Results and Discussion

Western Lake Erie is polymictic, meaning that it does not continuously stratify during the summer owing to shallow bathymetry and exposure to wind. Temperature profiles simulated by FVCOM show periods of temporary stratification that are strongest during calm afternoons when the surface is warmed by the sun and warm summer air (Figure 2a, 19–20 August). At night, cooling of the surface often causes deepening of the surface mixed layer by convection. This diel cycle can be overpowered by shear-induced mixing during windy periods (Figure 2a, 21–22 August). The temperature difference over the water column during periods of stratification is small (Figure 2a), but the static stability is sufficient to cause turbulent diffusivity to vary by orders of magnitude over a depth range of a few meters (Figure 2b). Random walk turbulence schemes are susceptible to formation of artificial accumulations of particles in the presence of strong gradients in diffusivity [*Visser*, 1997].

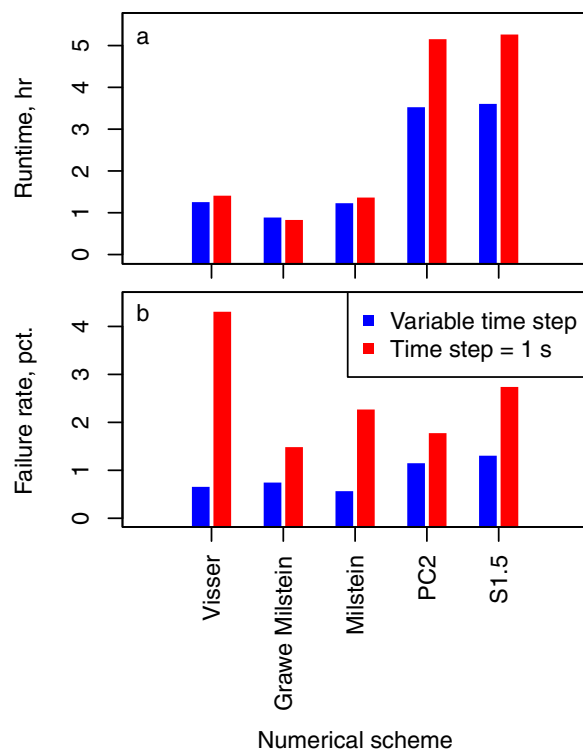


Figure 3. Performance comparison of the five vertical random walk numerical schemes and the variable time step scheme. One-dimensional vertical mixing simulations with 1000 particles were conducted for the month of August 2011, at the six stations indicated in Figure 1. (a) Total run time for the six simulations. (b) Percent occurrence of failure to meet the quality criterion out of 4464 hourly records. The quality criterion was a signal to noise ratio >5 where the signal was simulated normalized surface concentration with buoyancy (N93 3 Aug) and the noise was absolute deviation of the normalized surface concentration from 1.0 in a well-mixed condition test (without buoyancy). Concentration was normalized to the mean column concentration.

600 s, with typical hourly means of 0.2–3 s. At the 13-m deep station (NDBC45005) in the central basin, the water column was continuously stratified, and longer time steps could be used; hourly minimum values of the variable time step were typically 0.2–2 s, mean values were 3–30 s and maximum hourly values were constrained by the upper limit of 600 s.

Example time series of concentration profiles output from a well-mixed condition simulation are shown in Figure 2. A typical particle accumulation artifact is visible in Figure 2c, where the normalized concentration deviated from the expected constant value of unity. The artifact formed when high diffusivity in the surface mixed layer on 24 August (Figure 2b) caused particles to jump across the sharp diffusivity gradient into the area of low diffusivity in the lower half of the water column without the opportunity for the gradient term (equations (3) and (4)) to push the particles back toward the high diffusivity SML. Improved performance can be seen in Figure 2d, where the variable time step was reduced during the high diffusivity event on 24 August, thereby limiting the maximum particle displacements and reducing the magnitude of the artifact.

The Gräwe Milstein scheme [Gräwe, 2011] with the variable time step provided the best combination of computational efficiency and accuracy of the random-walk numerical schemes tested. The shortest run time was achieved by the Gräwe Milstein scheme (Figure 3a), which was unique in the use of linear interpolation of diffusivity to the particle position, while the other schemes used cubic splines at a greater computational cost. The second-order schemes, PC2 and S1.5, required greater computational effort to calculate additional terms and had the longest run times. The run time of the variable time step simulation was similar to that of the fixed 1 s time step for the Visser and Milstein schemes because the average of the variable time step was similar to the value of the fixed 1 s time step (Figure 3a). The

3.1. Vertical Random Walk Schemes

We tested the random walk schemes using a 1-D well-mixed condition simulation (see section 2) that was run using hourly time series of diffusivity profiles output from FVCOM for the month of August 2011 at stations representative of the range of conditions that occur during the summer CHAB season in western Lake Erie (Figure 1). The range of conditions represented by the diffusivity profiles can be characterized by defining a Peclet number that represents the ratio of mixing time scale to floating/sinking time scale of the water column, $Pe = w_b h / \bar{K}$, where h is the water column depth and \bar{K} is the column-mean eddy diffusivity [Ross and Sharples, 2004]. Values of $Pe \gg 1$ indicate that w_b has a strong influence on particle concentration profiles. Combining the time series of diffusivity profiles that was used in the well-mixed condition simulations with $w_b = 70 \mu\text{m s}^{-1}$ (see below), values ranged on the order of $0.01 < Pe < 100$. A small time step is usually required for $Pe \ll 1$ because small h and large \bar{K} will produce strong gradients in diffusivity for realistic diffusivity profiles (i.e., $K \sim 0$ at the bottom or at the thermocline), and therefore, small values of the Visser time step criterion (equation (5)). At the 3 m deep station (WE6), the variable time step occasionally was limited by the specified minimum and maximum values of 0.01 and

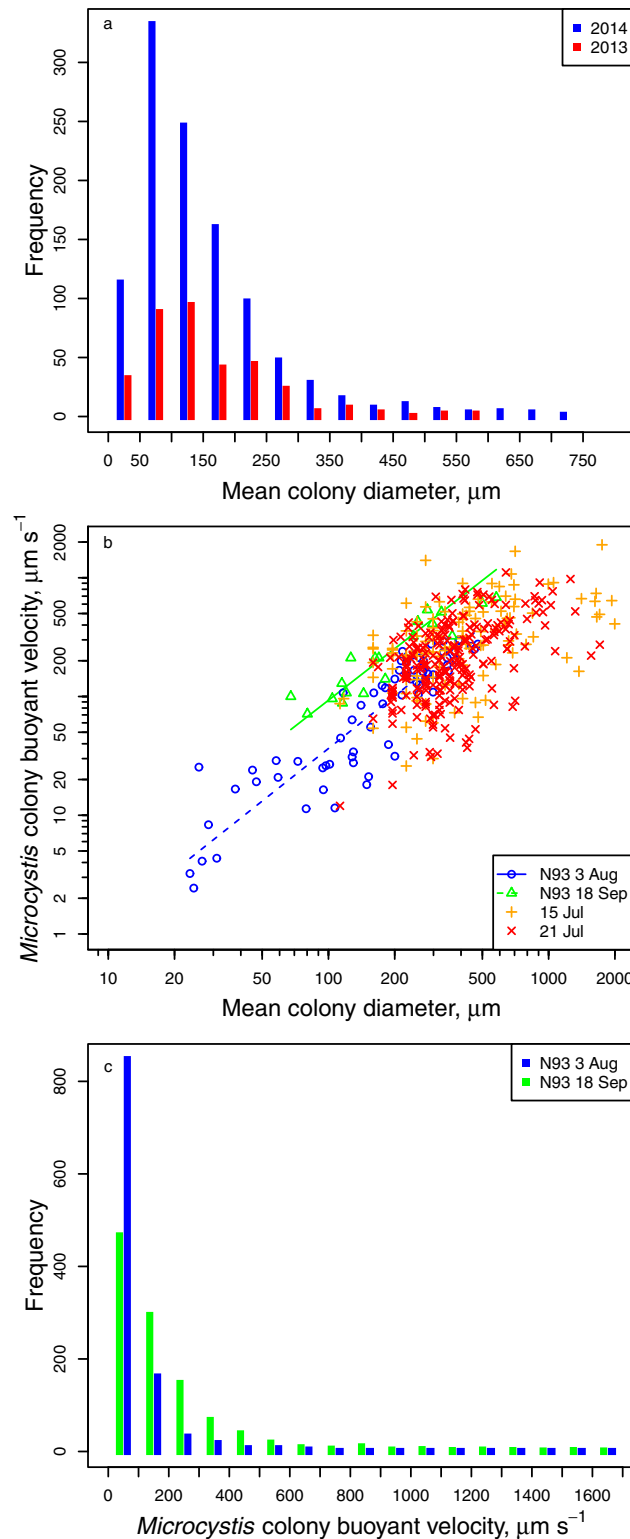


Figure 4. (a) Histogram of *Microcystis* colony size distribution for samples collected in Lake Erie in 2013 and 2014. (b) *Microcystis* colony buoyant velocity for samples collected in Lake Erie on 15 and 21 July 2015, and data digitized from Nakamura *et al.* [1993, their Figure 3]. (c) Histogram of *Microcystis* colony buoyant velocity resulting from application of the regression lines in Figure 2b to the 2015 size distribution in Figure 2a.

Milstein schemes showed improved accuracy compared to the Visser scheme with the fixed 1 s time step (Figure 3b), consistent with the finding of Gräwe [2011]. All schemes were more accurate with the variable time step than with the fixed 1 s time step (Figure 3b) because the Visser time step criterion (equation (5)) was always satisfied in the case of the variable time step. The second-order schemes did not offer sufficiently improved accuracy to compensate for their greater computational effort (Figures 3a and 3b).

In contrast to our result, Gräwe [2011] found that the second-order schemes did offer improved accuracy that justified the additional computational effort, but for the case of idealized diffusivity profiles specified at high vertical resolution and for a realistic test case of a tidally-mixed bay with model diffusivity output at 200 levels. In our case of a shallow polymictic lake, diffusivity profiles were highly irregular with sharp gradients (Figure 2b), and diffusivity was output at only 20 levels. We found that spline fits often had spurious features between the levels at which diffusivity was specified by FVCOM that were not representative of physically realistic diffusivity profiles. Higher order random walk schemes depend on higher order derivative terms from the spline fits to the diffusivity profiles [Gräwe, 2011], which may not be accurate in the case of a nonrepresentative spline fit. The higher order schemes might produce better results if we were to output diffusivity at a large number of levels, but that would come at the expense of greater computational effort in the hydrodynamic model. For our application, the Gräwe Milstein scheme produced satisfactory results and did not require a spline fit, so it was selected for further work.

3.2. *Microcystis* Colony Size Distribution and Buoyant Velocity

The parameter w_b represents the *Microcystis* colony terminal velocity resulting from the balance of forces between buoyancy and fluid drag. Our approach

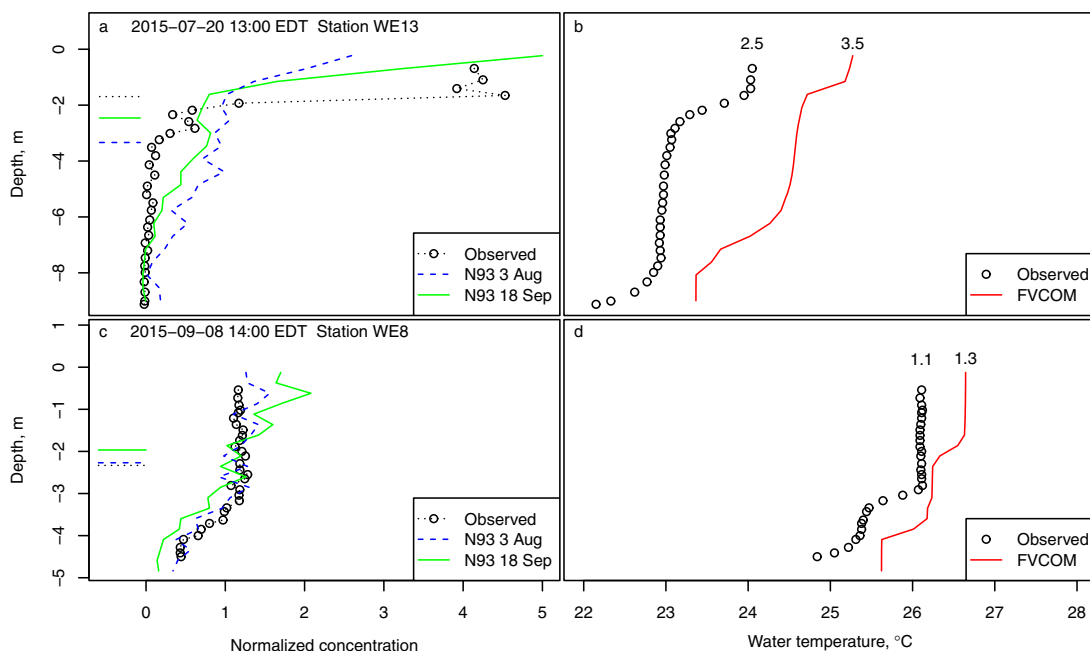


Figure 5. Two examples of observed vertical profiles of normalized concentration of cyanobacterial chlorophyll and temperature with simulated values plotted for comparison. Horizontal lines indicate the center of mass, σ_{mv} , of the normalized concentration profiles, and the potential energy anomaly, ϕ , J m^{-3} , is given above the temperature profiles.

was to specify a *Microcystis* colony size distribution, then apply an empirical relationship between w_b and colony diameter to obtain a frequency distribution of w_b for use in the model. According to Stoke's law for the terminal velocity of a floating/sinking spherical particle in a fluid, one might expect the relationship between w_b and colony diameter to give a straight line on a log-log plot with a slope of 2. However, Nakamura *et al.* [1993] showed that *Microcystis* colony specific gravity approaches that of the surrounding fluid as colony diameter increases owing to the fractal geometry of the colonies and the increasing volume of void spaces filled with the surrounding water; the result is that the slope of the log-log plot is <2 .

The *Microcystis* colony diameter frequency distribution measured by FlowCam was unimodal with a median of $117 \mu\text{m}$ and a maximum of $740 \mu\text{m}$ (Figure 4a, Station WE12, 4 August 2014). The size frequency distribution measured by microscopy on samples collected at stations WE 2, 4, 6, and 8 in July to October 2013 and June to July 2014 gave a similar size distribution to that of the 4 August 2014 sample (Figure 4a). It is likely that the colony size distribution varies to some extent spatially and temporally [e.g., Lin *et al.*, 2014], and our estimate could be refined through additional measurements. Even so, the consistency between our two estimated size distributions gives some indication of representativeness.

Our measured values of Lake Erie *Microcystis* colony buoyant velocity, w_b , were similar to those of Nakamura *et al.* [1993] for colonies larger than $200 \mu\text{m}$ in their sample collected from a lake in Japan on 3 August 1990, and generally less than their 18 September sample (Figure 4b). We were not able to resolve colonies smaller than $200 \mu\text{m}$ by our method; however, large colonies account for the majority of biomass and toxin concentration. For example, colonies $>112 \mu\text{m}$ accounted for 93% of *Microcystis* cells (biomass) in Lake Erie samples [Chaffin *et al.*, 2011], and colonies $>100 \mu\text{m}$ showed the highest proportion of microcystin-producing genotypes, highest microcystin cell quotas, and highest microcystin production rate, compared to smaller colony size classes in Lake Wannsee, Germany [Kurmayer *et al.*, 2003]. In addition to colony size, *Microcystis* buoyancy is a function of *Microcystis* strain and light exposure history, as it affects gas vacuole and carbohydrate content of the cells [Ibelings *et al.*, 1991; Xiao *et al.*, 2012]. Further research is necessary to define buoyant velocities over a wide size range of Lake Erie *Microcystis* under a variety of environmental conditions. Our results, while limited in size range, do show similarity between the $>200 \mu\text{m}$ values of Nakamura *et al.* [1993] and samples from two different dates in Lake Erie, and support using the lower estimate of buoyancy (Figure 4b, N93 3 Aug) from Nakamura *et al.* [1993].

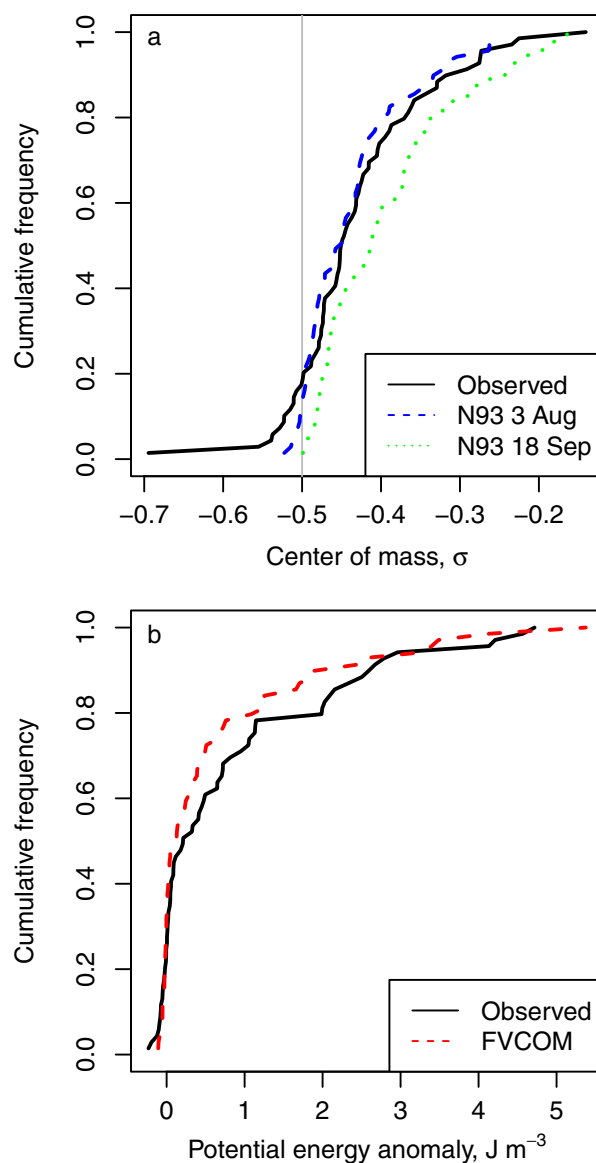


Figure 6. Cumulative frequency distributions of simulated and observed (a) center of mass of the normalized cyanobacteria concentration profile, and (b) potential energy anomaly of the temperature profile for 69 profiles collected in July to September of 2015 at stations indicated in Figure 1.

tion features can have a strong influence on diffusivity (e.g., Figures 2a and 2b). The accuracy of temperature simulations in hydrodynamic models is often only within a few degrees, which brings into question whether the subtle stratification features that are influencing the *Microcystis* vertical distribution can be reasonably simulated by a hydrodynamic model. Even though the simulated temperature profiles have a warm bias of 1–2°C, at these locations and times, they show thermoclines at multiple levels that are similar to the observed profiles (Figures 5b and 5d). The deeper thermocline may have formed due to convective deepening of the SML overnight, followed by surface warming during the day that produced the shallower thermocline; the profiles were captured in the afternoon. It is the static stability of the profile rather than the absolute temperature that is important in simulation of the diffusivity, and the static stability of the simulated and observed profiles is in reasonable agreement (Figures 5b and 5d). Over the full set of 69 profiles, the frequency distribution of static stability simulated by FVCOM was in reasonable agreement with the observed frequency distribution, although the model was biased slightly less stable than the observations (Figure 6b and Table 2).

For the model simulations, we assigned buoyant velocities to Lagrangian particles by random sampling with replacement from the frequency distributions shown in Figure 4c, which were obtained by applying the regression lines (Figure 4b) from the data of Nakamura *et al.* [1993] to the diameter frequency distribution from the 8 August 2014 sample from Lake Erie (Figure 4a). We tested the sensitivity of 1-D model simulations to the two buoyant velocity frequency distributions shown in Figure 2c, and refer to these hereafter as “N93 3 Aug” and “N93 18 Sep”. Example time series of concentration profiles simulated with the low estimate of buoyancy (N93 3 Aug) are shown in Figure 2e.

3.3. Vertical Profiles of Cyanobacterial Concentration and Temperature

We tested the ability of the random-walk model with buoyancy to simulate realistic *Microcystis* concentration profiles by comparing measured profiles of cyanobacterial chlorophyll concentration from Lake Erie (predominantly *Microcystis*) to corresponding 1-D simulations. On 20 July, the concentration profile showed strong accumulation within the surface two meters (Figure 5a), which corresponded to a surface mixed layer defined by a thermocline at 2 m depth (Figure 5b). A second profile was measured on 9 September, which showed concentration enrichment within a 3 m thick surface mixed layer (Figure 5c), which was similarly defined by a thermocline at 3 m depth (Figure 5d).

The temperature difference across the thermocline in both cases was only about 1°C (Figures 5b and 5d), but the FVCOM simulations indicated that such subtle stratifica-

tion features can have a strong influence on diffusivity (e.g., Figures 2a and 2b). The accuracy of temperature simulations in hydrodynamic models is often only within a few degrees, which brings into question whether the subtle stratification features that are influencing the *Microcystis* vertical distribution can be reasonably simulated by a hydrodynamic model. Even though the simulated temperature profiles have a warm bias of 1–2°C, at these locations and times, they show thermoclines at multiple levels that are similar to the observed profiles (Figures 5b and 5d). The deeper thermocline may have formed due to convective deepening of the SML overnight, followed by surface warming during the day that produced the shallower thermocline; the profiles were captured in the afternoon. It is the static stability of the profile rather than the absolute temperature that is important in simulation of the diffusivity, and the static stability of the simulated and observed profiles is in reasonable agreement (Figures 5b and 5d). Over the full set of 69 profiles, the frequency distribution of static stability simulated by FVCOM was in reasonable agreement with the observed frequency distribution, although the model was biased slightly less stable than the observations (Figure 6b and Table 2).

Table 2. Statistics Evaluating the Skill of the Lagrangian Particle Model in Simulating the Vertical Distribution of Cyanobacterial Chlorophyll Concentration (Center of Mass of the Normalized Concentration Profile) and of FVCOM in Simulating Temperature Profiles (Potential Energy Anomaly)^a

	Bias	RMSD	<i>r</i>
Center of mass, N93 18 Sep, σ	0.04	0.09	0.56
Center of mass, N93 3 Aug, σ	-0.01	0.08	0.53
Potential energy anomaly, $J m^{-3}$	-0.20	0.72	0.83

^aThe statistics are the mean bias, root mean square deviation (RMSD), and Pearson correlation coefficient (*r*).

Simulated normalized concentration profiles of buoyant particles showed enrichment within the surface mixed layer, similar to the observed profiles (Figures 5a and 5c). We calculated the center of mass, σ_m , of the concentration profile as a column-integrated indicator of the vertical distribution of concentration (horizontal lines in Figures 5a and 5c). Concentration was weighted toward the surface ($\sigma_m > -0.5$) in > 80% of the observed profiles (Figure 6a), which is consistent with the assumption to treat *Microcystis* colonies as buoyant particles in the model.

We selected the lower estimate of buoyancy (N93 3 Aug) for use in the hindcast simulations. The simulated frequency distribution of σ_m was in reasonable agreement with the observed distribution for both the low and high estimates of w_b , although the low estimate was closer to the observations (Figure 6a and Table 2). Similarly, the direct measurements of w_b also indicated better agreement with the lower estimate of buoyancy (Figure 4b).

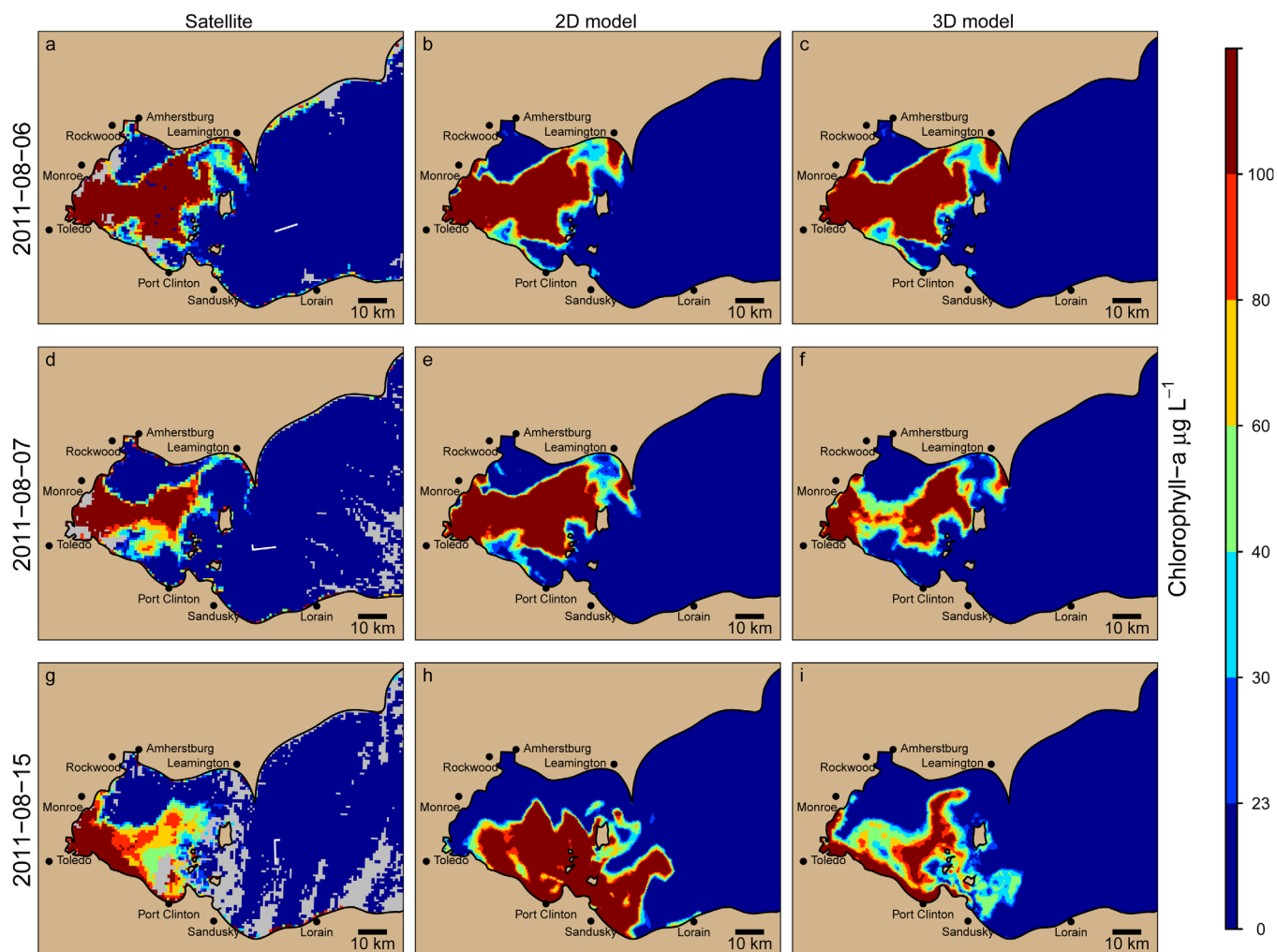


Figure 7. Comparison of 2-D and 3-D hindcast simulations initialized from satellite-derived cyanobacterial chlorophyll concentration (a) on 6 August 2011. (d, g) Subsequent satellite images were used for model skill assessment. Gray color indicates missing data. Wind speed, averaged over the preceding 12 h, was $<5 m s^{-1}$ on 6 August and increased to $5-10 m s^{-1}$ on 7 and 15 August (wind barbs a, d, g). In the 2-D simulation, particles were initiated in the surface 1 m and vertical mixing was not simulated (advection only). In the 3-D simulation, particles were initialized over the surface mixed layer, as determined by preliminary simulations of 1-D mixing with buoyancy, and the model was run with 3-D advection in addition to vertical mixing with buoyancy. While both 2-D and 3-D models simulated CHAB advection toward Port Clinton observed on 15 August, the 3-D model better simulated reduced intensity and coverage observed on 7 and 15 August due to higher winds, and continued CHAB coverage near Toledo and Monroe on 15 August.

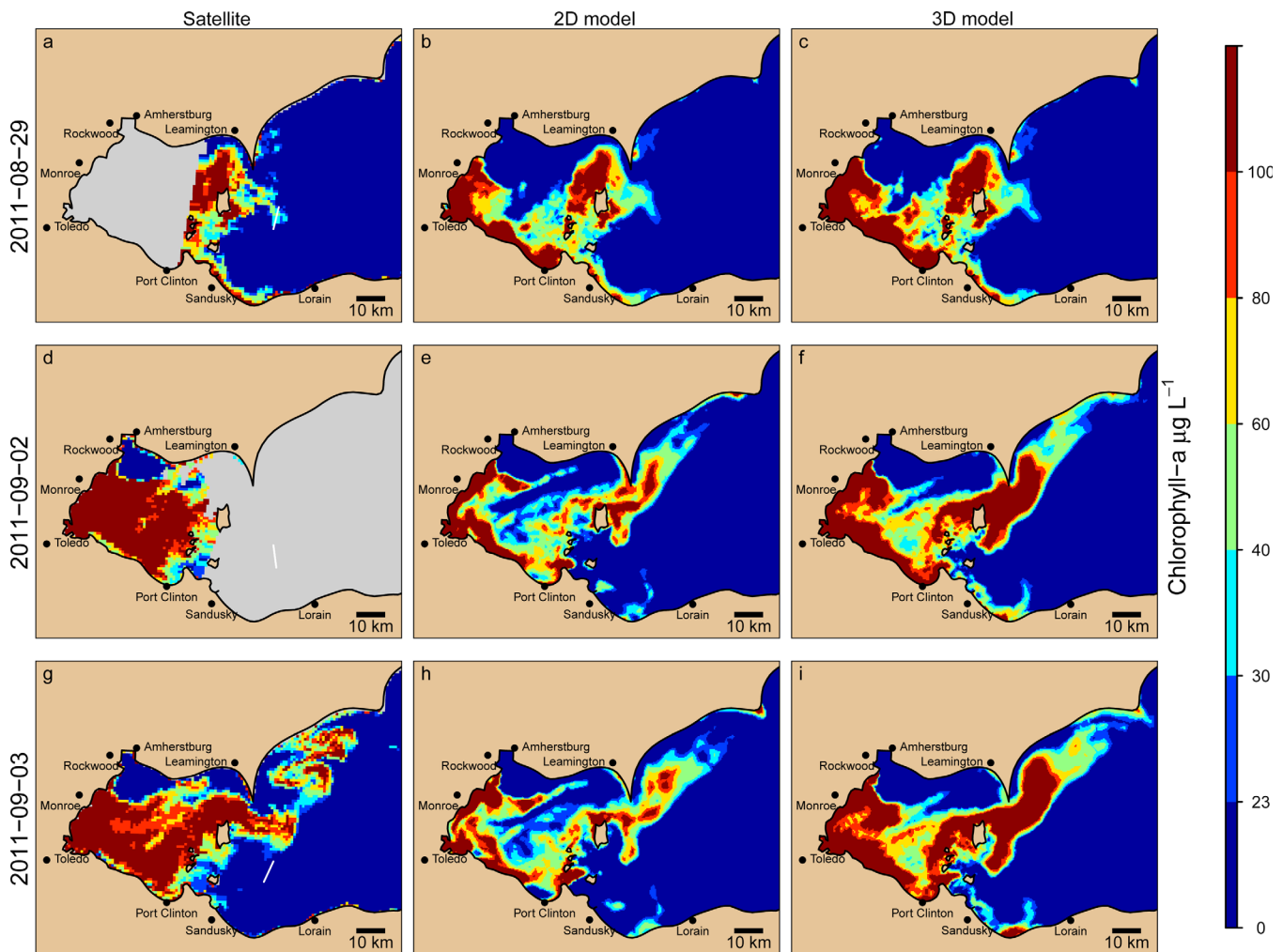


Figure 8. Comparison of 2-D and 3-D hindcast simulations initialized from satellite-derived cyanobacterial chlorophyll concentration (a) on 29 August 2011. Symbols and model setup are explained in Figure 7. While both 2-D and 3-D models simulated CHAB advection east of Leamington into the central basin observed on 3 September, the 3-D model better simulated CHAB intensity and extent in the western basin observed on 3 September. Wind speed was $<5 \text{ m s}^{-1}$ during the simulation period, but was north at 10 m s^{-1} until 12 h prior to the initial image.

3.4. Hindcast Simulations of CHAB Intensity and Distribution

Having shown that 1-D random walk simulations reasonably approximated the changing vertical distributions of buoyant *Microcystis* colonies in response to varying turbulence, we went on to test whether inclusion of this mechanism in the forecast model improved model skill. Hindcast simulations were initiated from each of the 26 quality satellite images of CHAB distribution for the 2011 CHAB season.

In one example, a hindcast simulation was initialized on 6 August, which was a calm day (wind $<5 \text{ m s}^{-1}$) with an intense CHAB event throughout the central western basin (Figure 7a). On the following day, wind increased ($5\text{--}10 \text{ m s}^{-1}$), and a second satellite image indicated reduced surface CHAB intensity and distribution (Figure 7d). The 3-D simulation captured the reduced surface CHAB intensity on 7 August, while the 2-D model did not, which can be seen qualitatively by comparing Figures 7e and 7f, and was indicated quantitatively by reduced frequency bias (B) of the 3-D simulation compared to the 2-D simulation (3-D B = 1.10; 2-D B = 1.34). On day 9 (15 August), the simulated CHAB distribution was distinctly different between the 2-D and 3-D models (Figures 7h and 7i). In comparison to the 2-D model, the 3-D model CHAB distribution was more similar to the observed distribution (3-D PSS = 0.56; 2-D PSS = 0.41), having less CHAB coverage in the central basin east of Sandusky and more continuous coverage along the coast from Monroe to Toledo. Both 2-D and 3-D models simulated the advection of CHAB to Port Clinton (Figures 7b, 7c and 7h, 7i), which was minimally affected by CHAB on 6 August and fully covered on 15 August (Figures 7a and 7g).

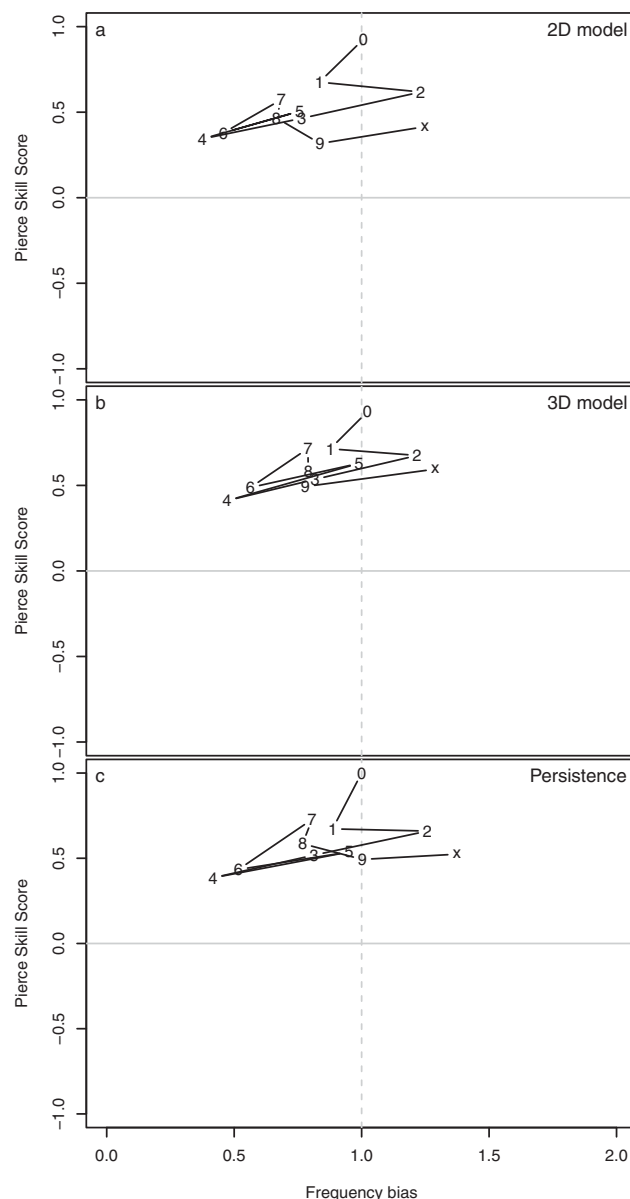


Figure 9. Skill-bias plots for the 2-D model (advection only), 3-D model (advection, vertical mixing, and buoyancy), and persistence forecasts for the 2011 hindcast simulations. The plot symbol indicates the simulation day (0 = initial, x = day 10). Pierce skill score (PSS) is the hit rate minus the false detection rate, and frequency bias (B) is the ratio of forecast hits to observed hits. Positive PSS indicates greater skill than a random forecast. Frequency bias of 1.0 indicates the same number of CHAB pixels were predicted as observed.

response to changing mixed layer depth. Finally, the 3-D model produced different final CHAB spatial distribution than the 2-D model, which likely results from the more accurate vertical distribution within a complex 3-D flow field.

3.5. Summary of Hindcast Skill Statistics

Skill statistics were summarized by simulation day to evaluate how long the model can be run from initialization before skill begins to decline. The Pierce skill score (PSS) gave positive values for the 2-D model, 3-D model, and the persistence forecast on simulation days 1–10 (Figure 9). Positive values of PSS indicate that the hit rate was greater than the false positive rate, and therefore the model had greater skill than a random forecast or constant CHAB or no-CHAB prediction [Hogan and Mason, 2012]. The frequency bias was less

In a second example, a hindcast simulation was initialized on 29 August, which was a date with only partial coverage by the satellite image, leaving no data over much of the western basin (Figure 8a). Output from a previous model run was used to initialize the CHAB distribution in the western basin (Figures 8b and 8c). On simulation day four (2 September) a second partial satellite image indicated extensive CHAB coverage in the western basin (Figure 8d), consistent with both models. Both 2-D and 3-D models underestimated the CHAB coverage, although the 3-D model better matched the observed coverage (2-D $B = 0.81$, $PSS = 0.76$; 3-D $B = 0.90$, $PSS = 0.84$; Figures 8d, 8e, and 8f). The partial image on 2 September did not show the extensive CHAB outbreak into the central basin east of Leamington, Ontario, although it was simulated by both 2-D and 3-D models (Figures 8e and 8f), and was revealed the following day in the 3 September satellite image (Figure 8g). The 3-D model better simulated the CHAB distribution on simulation day 5 (3 September) than the 2-D model (2-D $B = 0.79$, $PSS = 0.68$; 3-D $B = 0.99$, $PSS = 0.80$; Figures 8g, 8h, and 8i).

The examples in Figures 7 and 8 show, that both 2-D and 3-D models capture some observed events that may be attributed to advection, but the 3-D model performed better in several cases. The 3-D model is initialized with a better estimate of total biomass than the 2-D model because an estimate of the surface mixed layer depth for buoyant *Microcystis* colonies is used to assign the depth over which the satellite-derived surface concentration is applied. In addition, the 3-D model is able to simulate changing surface concentration in

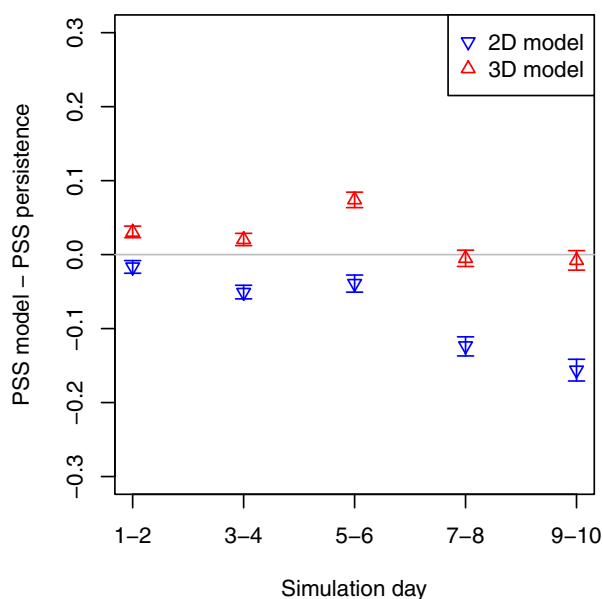


Figure 10. Pierce skill score (PSS) of the model minus PSS of the persistence forecast. Positive values indicate greater skill for the model than for the persistence forecast. Error bars indicate the 95% bootstrap confidence interval on the difference in PSS for the 26 hindcast simulations from the 2011 CHAB season, grouped into two-day intervals. The 3-D model (including vertical mixing with buoyancy) had greater skill than the 2-D model (advection only) and greater skill than the persistence forecast through day 6 and comparable skill out to day 10.

Erie CHAB spatial patterns compiled by Wynne and Stumpf [2015]. The model does not necessarily preserve these persistent features. For example, CHABs may be erroneously flushed from Maumee Bay in long simulations, although this happened to a lesser extent in the 3-D model than in the 2-D model (Figures 7g, 7h, and 7i). The skill of the persistence forecast indicates that the most recent satellite image is a reasonable indication of the CHAB distribution for several days after.

Skill statistics based on pixel-by-pixel comparisons, and use of a persistence forecast as a benchmark, provide a useful point of comparison among models, but do not capture all aspects of model performance. For example, the large simulated plume that extended into the central basin on 3 September (Figures 8g, 8h, and 8i) does not exactly match the observed plume in terms of shape and position. This pattern mismatch detracted from pixel-by-pixel skill statistics, but both models provided information regarding the existence of this transport event before it could be seen in satellite imagery; information that would be useful to forecast users even if the shape of the plume is not entirely accurate. A persistence forecast can score reasonably well in skill statistics that compare spatial patterns, but cannot provide any information on likely transport trajectories. Therefore, even though the 2-D model had less skill than the persistence forecast (Figure 10), this does not indicate that the 2-D model has no value because it may provide useful information on likely transport trajectories. It is a challenge to formulate skill statistics that test for accuracy in simulation of transport events, largely because it is difficult to identify and quantify transport events by comparing among subsequent satellite images. Wynne *et al.* [2011] attempted to calculate skill statistics based on movement of the bloom centroid; however, this approach is likely to work only for special cases because accurate calculation of the bloom centroid is sensitive to missing data (cloud cover) and the bloom often consists of multiple patches that may move in different directions rather than one distinct patch. Formulation of appropriate skill statistics for CHAB forecasts is an area for further work.

3.6. Ecological Significance

Aside from the specific application of CHAB forecasting, the observations and simulations shown here provide interesting insights on the physical processes that influence phytoplankton ecology in a polymictic lake. Previous studies of Lake Erie circulation and thermal structure considered the western basin to be largely unstratified [e.g., Beletsky *et al.*, 2013], but our study highlighted the importance of fine-scale thermal

than 1.0 on 8 of 10 forecast days, indicating that both models had an overall bias toward under-prediction, although not consistently so (Figures 9a and 9b). The 95% confidence intervals on the difference in PSS indicated that the 3-D model displayed significantly greater skill in the hindcast simulations than the persistence forecast through simulation day 6, and was not significantly worse than the persistence forecast through day 10 (Figure 10). The 3-D model had significantly greater skill than the 2-D model over the full simulation period. The 2-D model had significantly less skill than the persistence forecast on all simulation days (Figure 10).

It may be surprising that the persistence forecast displayed a reasonable level of skill. This can be explained in that the spatial distribution of CHABs in Lake Erie has a number of persistent features. For example CHABs often persist in the southern and western portions of the western basin, while they are rarely present in the Detroit River plume and in the central basin east of the islands, as indicated by 13 years of Lake

structure in the western basin in a biological context. Surface mixed layer depth varies hour by hour due to subtle features in the temperature profile caused by the diel cycle of surface heating and cooling, further modified by varying wind stress. Colony buoyancy is sufficient to keep *Microcystis* concentrated within the constantly changing surface mixed layer depth. The thermal structure is subtle in comparison to the continuous seasonal stratification that occurs in deeper lakes, and in the central and eastern basins of Lake Erie, but important nonetheless to the *Microcystis* vertical distribution. The position of *Microcystis* colonies in the water column is critical to their light exposure, nutrient acquisition, and ultimately to their ability to dominate the phytoplankton community, and produce toxic blooms.

Acknowledgments

M.D. Rowe received funding from the Great Lakes Restoration Initiative through the U.S. Environmental Protection Agency and National Oceanic and Atmospheric Administration. The FVCOM model and Lagrangian particle tracking model code are available from <http://fvcom.smast.umassd.edu/>. David Schwab, University of Michigan, modified the Lagrangian code for improved efficiency. Duane Gossiaux, NOAA GLERL, measured colony size distributions by microscopy. Danna Palladino and Ashley Burtner, CILER, collected field samples from Lake Erie in 2012, 2013, and 2014. We are grateful to Ulf Gräwe, Leibniz Institute for Baltic Sea Research, for providing code for alternative random walk numerical schemes. Data and model results are available upon request from the corresponding author (mark.rowe@noaa.gov). This is GLERL contribution 1825.

References

- Anderson, E. J., and M. S. Phanikumar (2011), Surface storage dynamics in large rivers: Comparing three-dimensional particle transport, one-dimensional fractional derivative, and multirate transient storage models, *Water Resour. Res.*, *47*, W09511, doi:10.1029/2010WR010228.
- Anderson, E. J., and D. J. Schwab (2013), Predicting the oscillating bi-directional exchange flow in the Straits of Mackinac, *J. Great Lakes Res.*, *39*(4), 663–671.
- Anderson, E. J., D. J. Schwab, and G. A. Lang (2010), Real-time hydraulic and hydrodynamic model of the St. Clair River, Lake St. Clair, Detroit River System, *J. Hydraul. Eng.*, *136*, 507.
- Anderson, E. J., A. J. Bechle, C. H. Wu, D. J. Schwab, G. E. Mann, and K. A. Lombardy (2015), Reconstruction of a meteotsunami in Lake Erie on 27 May 2012: Roles of atmospheric conditions on hydrodynamic response in enclosed basins, *J. Geophys. Res.*, *120*, 8020–8038, doi: 10.1002/2015JC010883.
- Bai, X., J. Wang, D. J. Schwab, Y. Yang, L. Luo, G. A. Leshkevich, and S. Liu (2013), Modeling 1993–2008 climatology of seasonal general circulation and thermal structure in the Great Lakes using FVCOM, *Ocean Modell.*, *65*, 40–63.
- Beletsky, D., D. Schwab, P. Roebber, M. McCormick, G. Miller, and J. Saylor (2003), Modeling wind-driven circulation during the March 1998 sediment resuspension event in Lake Michigan, *J. Geophys. Res. Oceans*, *108*(C2), 3038, doi:10.1029/2001JC001159.
- Beletsky, D., N. Hawley, and Y. R. Rao (2013), Modeling summer circulation and thermal structure of Lake Erie, *J. Geophys. Res. Oceans*, *118*, 6238–6252, doi:10.1002/2013JC008854.
- Bridgeman, T. B., J. D. Chaffin, and J. E. Filbrun (2013), A novel method for tracking western Lake Erie *Microcystis* blooms, 2002–2011, *J. Great Lakes Res.*, *39*(1), 83–89.
- Brittain, S. M., J. Wang, L. Babcock-Jackson, W. W. Carmichael, K. L. Rinehart, and D. A. Culver (2000), Isolation and characterization of microcystins, cyclic heptapeptide hepatotoxins from a Lake Erie strain of *Microcystis aeruginosa*, *J. Great Lakes Res.*, *26*(3), 241–249.
- Bundy, M. H., T. F. Gross, H. A. Vanderploeg, and J. R. Strickler (1998), Perception of inert particles by calanoid copepods: Behavioral observations and a numerical model, *J. Plankton Res.*, *20*(11), 2129–2152.
- Catherine, A., N. Escoffier, A. Belhocine, A. Nasri, S. Hamlaoui, C. Yéprémian, C. Bernard, and M. Troussellier (2012), On the use of the FluoroProbe®, a phytoplankton quantification method based on fluorescence excitation spectra for large-scale surveys of lakes and reservoirs, *Water Res.*, *46*(6), 1771–1784.
- Chaffin, J. D., T. B. Bridgeman, S. A. Heckathorn, and S. Mishra (2011), Assessment of *Microcystis* growth rate potential and nutrient status across a trophic gradient in western Lake Erie, *J. Great Lakes Res.*, *37*(1), 92–100.
- Chen, C., H. Liu, and R. C. Beardsley (2003), An unstructured grid, finite-volume, three-dimensional, primitive equations ocean model: Application to coastal ocean and estuaries, *J. Atmos. Oceanic Technol.*, *20*(1), 159–186.
- Chorus, I., and J. Bartram, Eds. (1999), Toxic Cyanobacteria in Water—A Guide to Their Public Health Consequences, Monitoring, and Management, E & FN Spon, published on behalf of the World Health Organization, U. K.
- Churchill, J. H., J. Runge, and C. Chen (2011), Processes controlling retention of spring-spawned Atlantic cod (*Gadus morhua*) in the western Gulf of Maine and their relationship to an index of recruitment success, *Fish. Oceanogr.*, *20*(1), 32–46.
- Galperin, B., L. Kantha, S. Hassid, and A. Rosati (1988), A quasi-equilibrium turbulent energy model for geophysical flows, *J. Atmos. Sci.*, *45*(1), 55–62.
- Gilbert, C., W. Gentleman, C. Johnson, C. DiBacco, J. Pringle, and C. Chen (2010), Modelling dispersal of sea scallop (*Placopecten magellanicus*) larvae on Georges Bank: The influence of depth-distribution, planktonic duration and spawning seasonality, *Prog. Oceanogr.*, *87*(1), 37–48.
- GLWQA Annex 4 (2015), Recommended phosphorus loading targets for Lake Erie, annex 4 objectives and targets task team final report to the nutrients annex subcommittee, 70 pp. [Available at <http://www.epa.gov/glwqa>.]
- Gräwe, U. (2011), Implementation of high-order particle-tracking schemes in a water column model, *Ocean Modell.*, *36*(1), 80–89.
- Gräwe, U., E. Deleersnijder, S. H. A. M. Shah, and A. W. Heemink (2012), Why the Euler scheme in particle tracking is not enough: The shallow-sea pycnocline test case, *Ocean Dyn.*, *62*(4), 501–514.
- Henry, T. (2014), Toledo seeks return to normalcy after do not drink water advisory lifted, *Toledo Blade*, 5 August. [Available at <http://www.toledoblade.com/local/2014/08/05/Toledo-seeks-return-to-normalcy-after-do-not-drink-water-advisory-lifted.html>.]
- Hogan, R. J., and I. B. Mason (2012), Deterministic forecasts of binary events, in *Forecast Verification: A Practitioner's Guide in Atmospheric Science*, 2nd ed., pp. 31–59, John Wiley & Sons, Ltd., West Sussex, U. K.
- Huret, M., J. Runge, C. Chen, G. Cowles, Q. Xu, and J. Pringle (2007), Dispersal modeling of fish early life stages: Sensitivity with application to Atlantic cod in the western Gulf of Maine, *Mar. Ecol. Prog. Ser.*, *347*, 261–274.
- Ibelings, B. W., L. R. Mur, and A. E. Walsby (1991), Diurnal changes in buoyancy and vertical distribution in populations of *Microcystis* in two shallow lakes, *J. Plankton Res.*, *13*(2), 419–436.
- Kane, D. D., J. D. Conroy, R. P. Richards, D. B. Baker, and D. A. Culver (2014), Re-eutrophication of Lake Erie: Correlations between tributary nutrient loads and phytoplankton biomass, *J. Great Lakes Res.*, *40*(3), 496–501.
- Kring, S. A., S. E. Figary, G. L. Boyer, S. B. Watson, and M. R. Twiss (2014), Rapid in situ measures of phytoplankton communities using the bbe FluoroProbe: Evaluation of spectral calibration, instrument intercompatibility, and performance range, *Can. J. Fish. Aquat. Sci.*, *71*(7), 1087–1095.
- Kurmayer, R., G. Christiansen, and I. Chorus (2003), The abundance of microcystin-producing genotypes correlates positively with colony size in *Microcystis* sp. and determines its microcystin net production in Lake Wannsee, *Appl. Environ. Microbiol.*, *69*(2), 787–795.

- Lake Erie LaMP. (2011), Lake Erie Binational Nutrient Management Strategy: Protecting Lake Erie by Managing Phosphorus. Prepared by the Lake Erie LaMP Work Group Nutrient Management Task Group.
- Lin, L., G. Appiah-Sefah, and M. Li (2014), Using a laser particle analyzer to demonstrate relationships between wind strength and *Microcystis* colony size distribution in Lake Taihu, China, *J. Freshwater Ecol.*, *30*(3), 425–433, doi:10.1080/02705060.2014.976666.
- Medrano, E. A., R. Uittenbogaard, L. D. Pires, B. van de Wiel, and H. Clercx (2013), Coupling hydrodynamics and buoyancy regulation in *Microcystis aeruginosa* for its vertical distribution in lakes, *Ecol. Modell.*, *248*, 41–56, doi:10.1016/j.ecolmodel.2012.08.029.
- Michalak, A. M., E. J. Anderson, D. Beletsky, S. Boland, N. S. Bosch, T. B. Bridgeman, J. D. Chaffin, K. Cho, R. Confesor, and I. Daloğlu (2013), Record-setting algal bloom in Lake Erie caused by agricultural and meteorological trends consistent with expected future conditions, *Proc. Natl. Acad. Sci. U. S. A.*, *110*(16), 6448–6452.
- Nakamura, T., Y. Adachi, and M. Suzuki (1993), Flotation and sedimentation of a single *Microcystis* floc collected from surface bloom, *Water Res.*, *27*(6), 979–983.
- Obenour, D. R., A. D. Gronewold, C. A. Stow, and D. Scavia (2014), Using a Bayesian hierarchical model to improve Lake Erie cyanobacteria bloom forecasts, *Water Resour. Res.*, *50*, 7847–7860, doi:10.1002/2014WR015616.
- O’Neil, J., T. W. Davis, M. A. Burford, and C. Gobler (2012), The rise of harmful cyanobacteria blooms: The potential roles of eutrophication and climate change, *Harmful Algae*, *14*, 313–334, doi:10.1016/j.hal.2011.10.027.
- Rinta-Kanto, J. M., E. A. Konopko, J. M. DeBruyn, R. A. Bourbonniere, G. L. Boyer, and S. W. Wilhelm (2009), Lake Erie *Microcystis*: Relationship between microcystin production, dynamics of genotypes and environmental parameters in a large lake, *Harmful Algae*, *8*(5), 665–673.
- Rose, A. (1948), The sensitivity performance of the human eye on an absolute scale, *J. Opt. Soc. Am.*, *38*(2), 196–208, doi:10.1364/JOSA.38.000196.
- Ross, O. N., and J. Sharples (2004), Recipe for 1-D Lagrangian particle tracking models in space-varying diffusivity, *Limnol. Oceanogr. Methods*, *2*(9), 289–302.
- Ross, O. N., and J. Sharples (2008), Swimming for survival: A role of phytoplankton motility in a stratified turbulent environment, *J. Mar. Syst.*, *70*(3), 248–262.
- Simpson, J., and D. Bowers (1981), Models of stratification and frontal movement in shelf seas, *Deep Sea Res., Part A*, *28*(7), 727–738.
- Smagorinsky, J. (1963), General circulation experiments with the primitive equations: I. The basic experiment, *Mon. Weather Rev.*, *91*(3), 99–164.
- Strickler, J. R. (1985), Feeding currents in calanoid copepods: Two new hypotheses, in *Physiological Adaptations of Marine Animals*, edited by M. S. Laverack, pp. 459–485, Soc. for Exp. Biol., U. K.
- Stumpf, R. P., and T. T. Wynne (2015), Experimental Lake Erie harmful algal bloom bulletin (Bulletin 27). [Available at www2.nccos.noaa.gov/coast/lakeerie/bulletin/]
- Stumpf, R. P., T. T. Wynne, D. B. Baker, and G. L. Fahnenstiel (2012), Interannual variability of cyanobacterial blooms in Lake Erie, *PLoS One*, *7*(8), e42444, doi:10.1371/journal.pone.0042444.
- Tomlinson, M. C., R. P. Stumpf, T. T. Wynne, D. Dupuy, R. Burks, J. Hendrickson, and R. S. Fulton III (2016), Relating chlorophyll from cyanobacteria-dominated inland waters to a MERIS bloom index, *Remote Sens. Lett.*, *7*(2), 141–149.
- Vanderploeg, H. A., J. R. Liebig, W. W. Carmichael, M. A. Agy, T. H. Johengen, G. L. Fahnenstiel, and T. F. Nalepa (2001), Zebra mussel (*Dreissena polymorpha*) selective filtration promoted toxic *Microcystis* blooms in Saginaw Bay (Lake Huron) and Lake Erie, *Can. J. Fish. Aquat. Sci.*, *58*(6), 1208–1221.
- Visser, A. (1997), Using random walk models to simulate the vertical distribution of particles in a turbulent water column, *Mar. Ecol. Prog. Ser.*, *158*, 275–281.
- Wang, C., X. Wu, C. Tian, Q. Li, Y. Tian, B. Feng, and B. Xiao (2015), A quantitative protocol for rapid analysis of cell density and size distribution of pelagic and benthic *Microcystis* colonies by FlowCAM, *J. Appl. Phycol.*, *27*(2), 711–720.
- Wiles, P., L. van Duren, C. Häse, J. Larsen, and J. Simpson (2006), Stratification and mixing in the Limfjorden in relation to mussel culture, *J. Mar. Syst.*, *60*(1), 129–143.
- Wynne, T. T., and R. P. Stumpf (2015), Spatial and temporal patterns in the seasonal distribution of toxic cyanobacteria in Western Lake Erie from 2002–2014, *Toxins*, *7*(5), 1649–1663.
- Wynne, T., R. Stumpf, M. Tomlinson, R. Warner, P. Tester, J. Dyble, and G. Fahnenstiel (2008), Relating spectral shape to cyanobacterial blooms in the Laurentian Great Lakes, *Int. J. Remote Sens.*, *29*(12), 3665–3672.
- Wynne, T. T., R. P. Stumpf, M. C. Tomlinson, and J. Dyble (2010), Characterizing a cyanobacterial bloom in western Lake Erie using satellite imagery and meteorological data, *Limnol. Oceanogr. Methods*, *55*(5), 2025–2036.
- Wynne, T. T., R. P. Stumpf, M. C. Tomlinson, D. J. Schwab, G. Y. Watabayashi, and J. D. Christensen (2011), Estimating cyanobacterial bloom transport by coupling remotely sensed imagery and a hydrodynamic model, *Ecol. Appl.*, *21*(7), 2709–2721.
- Wynne, T. T., R. P. Stumpf, M. C. Tomlinson, G. L. Fahnenstiel, J. Dyble, D. J. Schwab, and S. J. Joshi (2013), Evolution of a cyanobacterial bloom forecast system in western Lake Erie: Development and initial evaluation, *J. Great Lakes Res.*, *39*, 90–99.
- Xiao, Y., N. Gan, J. Liu, L. Zheng, and L. Song (2012), Heterogeneity of buoyancy in response to light between two buoyant types of cyanobacterium *Microcystis*, *Hydrobiologia*, *679*(1), 297–311.